Monthly Notices
of the
ROYAL ASTRONOMICAL SOCIETY

MNRAS **480,** 26–34 (2018)
Advance Access publication 2018 July 9

doi:10.1093/mnras/sty1806

X-ray background and its correlation with the 21 cm signal

Q. Ma,[1,2,3,4★] B. Ciardi,[2] M. B. Eide[2] and K. Helgason[2,5]

[1]*Purple Mountain Observatory, Chinese Academy of Sciences, Nanjing 210008, China*
[2]*Max-Planck-Institut für Astrophysik, Karl-Schwarzschild-Straße 1, D-85748 Garching bei München, Germany*
[3]*Guizhou Provincial Key Laboratory of Radio Astronomy and Data Processing, Guizhou Normal University, Guiyang 550001, China*
[4]*University of Chinese Academy of Sciences, Beijing 100049, China*
[5]*Centre for Astrophysics and Cosmology, University of Iceland, Dunhagi 5, 107 Reykjavík, Iceland*

Accepted 2018 June 26. Received 2018 June 3; in original form 2018 April 12

ABSTRACT

We use high-resolution hydrodynamical simulations to study the contribution to the X-ray background from high-z energetic sources, such as X-ray binaries, accreting nuclear black holes, and shock heated interstellar medium. Adopting the model discussed in Eide et al. (2018), we find that these X-ray sources during the Epoch of Reionization (EoR) contribute less than a few per cent of the unresolved X-ray background. The same sources contribute to less than ∼2 per cent of the measured angular power spectrum of the fluctuations of the X-ray background. The outputs of radiative transfer simulations modeling the EoR are used to evaluate the cross-correlations of X-ray background with the 21 cm signal from neutral hydrogen. Such correlation could be used to confirm the origin of the 21 cm signal, as well as give information on the properties of the X-ray sources during the EoR. We find that the correlations are positive during the early stages of reionization when most of the hydrogen is neutral, while they become negative when the intergalactic medium gets highly ionized, with the transition from positive to negative depending on both the X-ray model and the scale under consideration. With SKA as the reference instrument for the 21 cm experiment, the predicted S/N for such correlations is <1 if the corresponding X-ray survey is only able to resolve and remove X-ray sources with observed flux $> 10^{-15}$ erg cm^{-2} s^{-1}, while the cumulative S/N from $l = 1000$ to 10^4 at $x_{\rm HI} = 0.5$ is ∼5 if sources with observed flux $> 10^{-17}$ erg cm^{-2} s^{-1} are detected.

Key words: galaxies: high-redshift – dark ages, reionization, first stars – X-rays: diffuse background.

1 INTRODUCTION

The combined contribution of radiation from sources at all redshifts makes up the background radiation permeating our universe. The X-ray component of such background includes input from a variety of high-energy sources (e.g. Brandt & Hasinger 2005; Helgason et al. 2014; Cappelluti et al. 2017), such as X-ray binaries (XRBs) (Fragos et al. 2013a), active galactic nuclei (AGNs) (Comastri et al. 1995), and thermal bremsstrahlung from hot gas (Cappelluti et al. 2012).

Deep X-ray surveys (Lehmer et al. 2012; Luo et al. 2017) have resolved most of the cosmic X-ray background (CXB) as point sources that are dominated by AGNs, while ∼10–30 per cent of the flux remains unresolved (see e.g. Lehmer et al. 2012; Moretti et al. 2012; Cappelluti et al. 2017). More specifically, the 4Ms *Chandra* Deep Field-South (CDF-S) (Lehmer et al. 2012) showed that this component amounts to 24.3 per cent of the total flux in the soft (0.5-2) keV band (i.e. $8.15 \pm 0.58 \times 10^{-12}$ erg cm^{-2} s^{-1} deg^{-2}) and 17.6 per cent in the hard (2-8) keV band (i.e. $1.73 \pm 0.23 \times 10^{-11}$ erg cm^{-2} s^{-1} deg^{-2}), which is composed by very faint sources that lay below the sensitivity of the instrument. Although these faint sources cannot be singly resolved, the imprint of their angular fluctuations on the CXB could provide some information on their properties (Yamamoto & Sugiyama 1998; Śliwa, Soltan & Freyberg 2001; Kolodzig et al. 2017, 2018). Specifically, measurements of cross-correlation with the near-infrared background indicate that such fluctuations should partially come from the high-z universe (Cappelluti et al. 2012; Helgason et al. 2014; Fernandez et al. 2014; Mitchell-Wynne et al. 2016).

It has been suggested that this high-z component could originate from accretion powered sources during the epoch of reionization (EoR), such as XRBs (Fragos et al. 2013a,b; Xu et al. 2016), and/or AGNs (Dijkstra, Haiman & Loeb 2004; Salvaterra et al. 2005; Salvaterra, Haardt & Volonteri 2007). Although they are also expected

★ E-mail: maqb@mpa-garching.mpg.de

© 2018 The Author(s)
Published by Oxford University Press on behalf of the Royal Astronomical Society

Downloaded from https://academic.oup.com/mnras/article-abstract/480/1/26/5050917 by National and University Library of Iceland user on 03 October 2019

to contribute to the CXB, it is not possible to separate such components directly from the CXB measurements due to the lack of redshift information. Since these sources are usually hosted in very dense regions, they are expected to anticorrelate with the 21 cm signal originating from the neutral hydrogen found further away from the production sites of ionizing photons (Shan & Qin 2009; Liang, Mao & Qin 2016). Exploiting the redshift information offered by the 21 cm signal, such cross-correlation could then be used to give information on the properties of the X-ray sources during the EoR, as well as confirm the origin of the 21 cm signal. It should be noted that the high-z component of the X-ray background is mainly contributed by the hard X-ray radiation that can easily escape from the hosts and travel large distances, while the soft X-ray photons produced by the same sources are expected to interact with the neutral hydrogen and helium and impact the physical properties of the intergalactic medium (IGM), and thus the associated 21 cm signal (Christian & Loeb 2013; Mesinger, Ferrara & Spiegel 2013; Fialkov, Barkana & Visbal 2014; Fialkov et al. 2017; Eide et al. 2018).

In this paper, we will evaluate the contribution to the CXB from high-z energetic sources such as XRBs, accreting nuclear black holes (BHs), and shock heated interstellar medium (ISM). The properties of the sources are retrieved from the hydrodynamic simulation MassiveBlack-II (Khandai et al. 2015). We also employ the 3D multifrequency radiative transfer (RT) code CRASH (Ciardi et al. 2001; Maselli, Ciardi & Kanekar 2009; Graziani, Ciardi & Glatzle 2018) to follow the reionization history of hydrogen and helium (Eide et al. 2018 and Eide et al. in preparation). These simulations are used to evaluate the 21 cm signal and the cross-correlation with the CXB for several source models. As mentioned above, such correlations were previously investigated by Shan & Qin (2009) by means of two semi-analytic models for reionization (stars dominated or quasars dominated), and by Liang et al. (2016) using seminumerical 21CMFAST simulations that included three cases of X-ray emitting efficiency. Both works concluded that a cross-correlation between X-ray background and 21 cm signal exists, although it is difficult to measure. Ours is the first work that attacks the problem employing a combination of hydrodynamic and radiative transfer simulations.

The rest of paper is organized as follows. Simulations and X-ray models adopted are described in Section 2; the results are presented in Section 3, while the conclusions are summarized in Section 4. The cosmological parameters adopted are from WMAP7 (Komatsu et al. 2011) within a ΛCDM cosmology, i.e. $\sigma_8 = 0.816$, $n_s = 0.968$, $\Omega_\Lambda = 0.725$, $\Omega_m = 0.275$, $\Omega_b = 0.046$ and $h = 0.701$.

2 SIMULATIONS

The simulations used to compute X-ray background and 21 cm signal are those described in Eide et al. (2018, hereafter Eide18a) and Eide et al. (in preparation, hereafter Eide18b). Here we outline their main characteristics and refer the reader to the original papers for more details.

The gas and galaxy distribution adopted, together with their properties, are obtained from the high-resolution cosmological hydrodynamical simulation MBII presented in Khandai et al. (2015), with box length $100\,h^{-1}$cMpc and 2×1792^3 particles, i.e. a dark matter and gas particle mass of $m_{\rm DM} = 1.1 \times 10^7\,h^{-1}$ M$_\odot$ and $m_{\rm gas} = 2.2 \times 10^6\,h^{-1}$ M$_\odot$, respectively. The simulation tracks stellar populations, galaxies, accreting and dormant BHs (growing from seeds of 10^5 M$_\odot$ by merging with other BHs and by accreting gas at a maximum of twice the Eddington rate), as well as their properties, such as mass, age, metallicity, accretion rate, and star formation rate (SFR). The baryonic physics and feedback effects of the sources are also accounted for. We refer the reader to Khandai et al. (2015) for more details about the hydrodynamical simulations. Here we just note that the parameters involved in the calculations have been tuned to reproduce low redshift observations, such as the cosmic SFR, the galaxy stellar mass function, and the quasar (QSO) bolometric luminosity function.

The outputs of the simulations have been mapped onto $N_c = 256^3$ grids and post-processed with the Monte Carlo 3D RT code CRASH (Ciardi et al. 2001; Maselli, Ferrara & Ciardi 2003; Maselli et al. 2009; Graziani, Maselli & Ciardi 2013) to follow the redshift evolution of the ionization and temperature state of the IGM, i.e. the reionization process, as determined by different source types (and their combination) emitting in the energy range 13.6–2 keV. In addition to stellar-type sources that emit the bulk of their radiation in the UV band, Eide18a,b considered the contribution to the production of more energetic photons from the following.

(i) *X-ray binaries (XRBs)*. These include low mass XRBs (LMXBs) and high mass XRBs (HMXBs). The corresponding total luminosity in a galaxy is given by the contribution from both populations: $L^{\rm XRB} = L^{\rm HMXB} + L^{\rm LMXB}$. The luminosity of HMXBs relates to the SFR of the galaxy and the metallicity (Z) of the residing stars as (Fragos et al. 2013b; Madau & Fragos 2017):

$$\log(L^{\rm HMXB}/{\rm SFR}) = \sum_i \beta_i Z^i, \tag{1}$$

while the luminosity of LMXBs is determined by the mass (M) and age (t) of the stars:

$$\log(L^{\rm LMXB}/M) = \sum_i \gamma_i (\log t)^i, \tag{2}$$

where β_i and γ_i denote the best-fitting coefficients from Madau & Fragos (2017).
The spectra of the XRB sources, which are only mildly dependent on the redshift, are taken from Fragos et al. (2013b).

(ii) *Supernova heated ISM*. For each galaxy, the luminosity of the ISM in the energy band (0.3–10) keV is evaluated as (Mineo, Gilfanov & Sunyaev 2012):

$$L^{\rm ISM} = (7.3 \pm 1.3) \times 10^{39}\,{\rm erg\,s^{-1}\,M_\odot^{-1}\,yr} \times {\rm SFR}, \tag{3}$$

where SFR is the total SFR in the galaxy. The luminosity is then rescaled to the frequency range of our interest.
We assume that the ISM spectrum is thermal bremsstrahlung and constant in redshift (Pacucci et al. 2014):

$$S^{\rm ISM}(\nu) = \begin{cases} C & \text{if } h_{\rm P}\nu \le kT_{\rm ISM} \\ C(h_{\rm P}\nu/kT_{\rm ISM})^{-3} & \text{if } h_{\rm P}\nu \ge kT_{\rm ISM} \end{cases} \tag{4}$$

where C is the normalization constant, $h_{\rm P}$ denotes the Planck constant, and $T_{\rm ISM} \sim 10^6$ K is the temperature of the heated ISM.

(iii) *Accreting nuclear BHs*. For each source we assume a bolometric luminosity (Shakura & Sunyaev 1973):

$$L^{\rm BH} = \eta \dot{M}_{\rm BH} c^2, \tag{5}$$

where $\eta = 0.1$ is the efficiency parameter used in Khandai et al. (2015) and $\dot{M}_{\rm BH}$ is the accretion rate of the BH computed in the simulations.
The spectrum is based on observational data by Krawczyk et al. (2013), which is modeled as a power law with index $\alpha = -1$ at $h_{\rm P}\nu > 200$ eV and has no evolution with redshift.

The suite of simulations used in this paper is composed of four runs from Eide18a and Eide18b, including stars and XRBs (XRB

Downloaded from https://academic.oup.com/mnras/article-abstract/480/1/26/5050917 by National and University Library of Iceland user on 03 October 2019

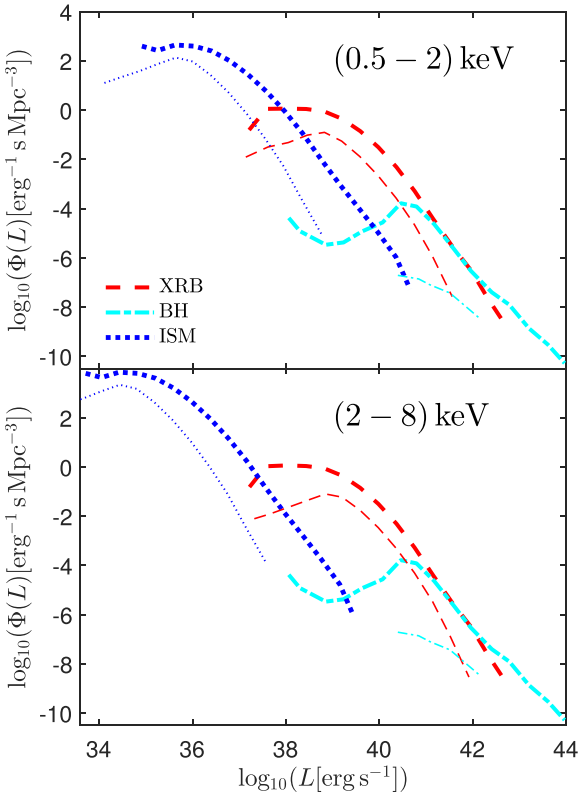

Figure 1. Intrinsic luminosity function in the observer frame frequency bands (0.5–2) keV (top panel) and (2–8) keV (bottom) as produced by our population of XRBs (red dashed lines), BHs (cyan dash-dotted), and ISM (blue dotted). Thick and thin lines refer to $z = 5$ and 10, respectively.

model), stars and ISM (ISM model), stars and BHs (BH model), and all of sources combined (referred to as 'Total' model). We refer the reader to the original papers for more details on the simulations.

It should be noted that in the RT simulations only photons with energies below 2 keV are included as the mean free path of the ones with higher energy is larger than the box size. Those soft X-ray photons do not contribute to the CXB, but Eide18a showed that they have an impact on the heating and ionization of the IGM, although full hydrogen ionization is driven by the UV radiation from stars.

3 RESULTS

Fig. 1 shows the intrinsic luminosity function of X-ray radiation as contributed by our population of XRBs, BHs, and ISM in the observer frame frequency bands (0.5–2) keV and (2–8) keV. The X-ray luminosity associated to the ISM is much lower than that of the others, while the BHs reach the highest luminosities, despite having the lowest number density. Due to its softer X-ray spectrum (i.e. $\propto \nu^{-3}$), the luminosity of the ISM is smaller in the (2–8) keV band than that in the (0.5–2) keV band, while the luminosities of XRBs and BHs are similar in the two bands.

As single X-ray sources at high redshift are too faint to be resolved as point sources (e.g. the observed flux for a source with $L = 10^{44}\,\mathrm{erg\,s^{-1}}$ at $z = 5$ is $3.6 \times 10^{-16}\,\mathrm{erg\,cm^{-2}\,s^{-1}}$), most of them only contribute to the unresolved CXB.[1]

3.1 Global X-ray flux

The global X-ray flux measured on earth from a source type s (XRB, BH or ISM) at redshift larger than z is expressed as

$$F^s(>z) = \frac{c}{4\pi}\int_{>z}\frac{\mathrm{d}z'}{H(z')}\frac{\langle L^s\rangle}{(1+z')^2}\int_{\nu_{\min}(1+z')}^{\nu_{\max}(1+z')}\mathrm{d}\nu S^s(\nu,z')\mathrm{e}^{-\tau(\nu,z')}, \quad (6)$$

where c is the speed of light, $H(z') = H_0\sqrt{\Omega_m(1+z')^3+\Omega_\Lambda}$ is the cosmic expansion rate at z', $\langle L^s\rangle$ is the averaged luminosity per unit volume, and $\tau(\nu, z')$ is the optical depth from z' to the observer for photons with frequency ν:

$$\tau(\nu,z') = \int_0^{z'}\frac{c\mathrm{d}z''}{(1+z'')H(z'')}\sum_m\sigma_m(\nu')\langle n_m\rangle(z''), \quad (7)$$

where $\nu' = \nu(1+z'')/(1+z')$, σ_m is the cross-section to X-ray photons for species m=H I, He I and He II (Verner et al. 1996), and $\langle n_m\rangle$ is the corresponding volume averaged number density as obtained in Eide18a and Eide18b. More specifically, $\langle n_m\rangle = \sum_c n_m^c/N_c$, where n_m^c is the number density of species m in cell c and it is evaluated from the gas number density and the ionization fractions of hydrogen and helium. As the simulations have been run only until full hydrogen reionization has been reached, $z_\mathrm{r} \sim 6$, we assume that at $z < z_\mathrm{r}$ hydrogen remains fully ionized, while for helium we assume that $x_{\mathrm{He\,II}}(3 < z < z_\mathrm{r}) = x_{\mathrm{He\,II}}(z_\mathrm{r})$, $x_{\mathrm{He\,II}}(z \le 3) = 0$, $x_{\mathrm{He\,III}}(3 < z < z_\mathrm{r}) = x_{\mathrm{He\,III}}(z_\mathrm{r})$, and $x_{\mathrm{He\,III}}(z \le 3) = 1$. As expected, the optical depth to the energetic photons of interest here is extremely low (e.g. $\tau < 0.0003$ for photons >0.5 keV in the observer frame at $z < 15$), thus it can be safely neglected.

Fig. 2 presents the predicted global X-ray flux in the observed (0.5–2) keV and (2–8) keV bands. For all models, the flux increases quickly with decreasing redshift, due to the fast growing of structures and the associated relevant physical properties, e.g. stellar mass, SFR, accreting BHs (see Eide2018a,b for further discussions). The XRB and BH models display X-ray fluxes very similar in the soft and hard bands due to their spectral index (for both it is ≈ -1), while the ISM model shows a lower flux in the hard band than in the soft band as a consequence of its softer spectrum (spectral index -3). As the flux in the Total model is dominated at all redshifts by the XRBs contribution, its behavior is similar to that of the XRB model.

In the soft (0.5–2) keV band, the flux from XRBs, BHs, and ISM at $z > 5$ is 8.18×10^{-14}, 1.99×10^{-14}, and $2.04 \times 10^{-16}\,\mathrm{erg\,cm^{-2}\,s^{-1}\,deg^{-2}}$, respectively, corresponding to 80.3 per cent, 19.5 per cent, and 0.2 per cent of the flux in the Total model, which is $1.02 \times 10^{-13}\,\mathrm{erg\,cm^{-2}\,s^{-1}\,deg^{-2}}$. In comparison, the unresolved CXB in the same band measured by Cappelluti et al. (2017) is $(2.90 \pm 0.16) \times 10^{-12}\,\mathrm{erg\,cm^{-2}\,s^{-1}\,deg^{-2}}$, while the unresolved X-ray flux inferred by Lehmer et al. (2012) is $(1.98 \pm 0.35) \times 10^{-12}\,\mathrm{erg\,cm^{-2}\,s^{-1}\,deg^{-2}}$, i.e. our predicted X-ray flux from the EoR is less than a few per cent of the unresolved CXB expected from observations.

Similarly, in the hard (2–8) keV band the flux from XRBs, BHs and ISM at $z > 5$ is 8.94×10^{-14}, 1.99×10^{-14}, and

[1]The brightest sources could be resolved in very deep observations with small fields of view (e.g. Lehmer et al. 2012; Luo et al. 2017), but it would be difficult to detect them in large-scale surveys (e.g. Cappelluti et al. 2012, 2013; Kolodzig et al. 2017).

Downloaded from https://academic.oup.com/mnras/article-abstract/480/1/26/5050917 by National and University Library of Iceland user on 03 October 2019

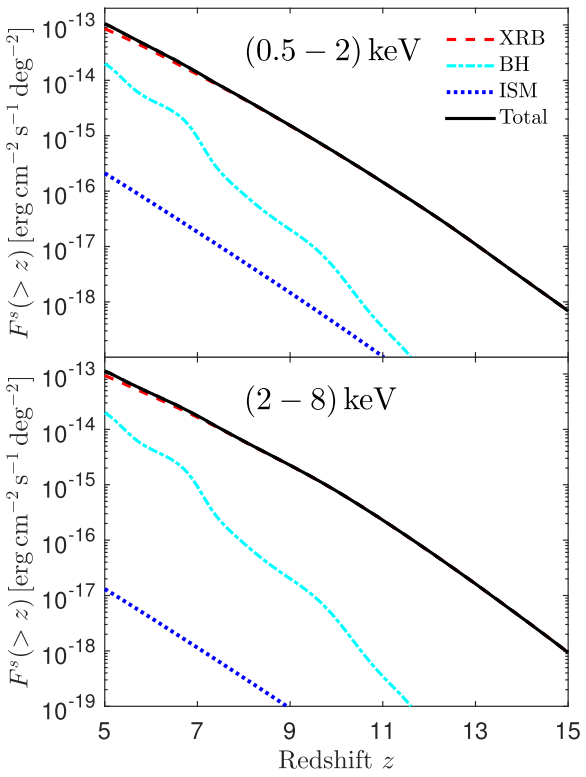

Figure 2. Integrated X-ray flux at $>z$ for source model XRB (dashed red lines), BH (dot-dashed cyan), ISM (dotted blue), and Total (solid black). The upper and lower panel refers to the energy band (0.5–2) keV and (2–8) keV, respectively.

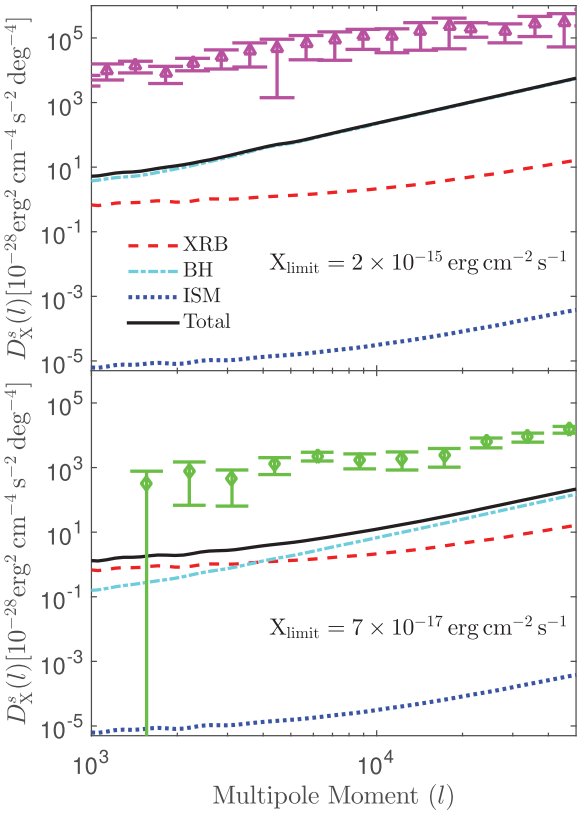

Figure 3. Angular power spectrum of the X-ray flux in the (0.5–2) keV band from $z > 5$. The lines refer to the XRB (dashed red lines), BH (dash-dotted cyan), ISM (dotted blue), and Total (solid black) model. The top panel is the power spectra obtained when bright sources with observed flux $\geq 2 \times 10^{-15}$erg cm^{-2} s^{-1} are removed, while the bottom panel removes bright sources with observed flux $\geq 7 \times 10^{-17}$erg cm^{-2} s^{-1}. The green diamond data points with error bars in the bottom panel are from Cappelluti et al. (2013) obtained with a flux limit of $\sim 7 \times 10^{-17}$erg cm^{-2} s^{-1}, while the magenta triangle ones in the top panel are from Kolodzig et al. (2017) obtained with a flux limit of $\sim 2 \times 10^{-15}$erg cm^{-2} s^{-1}.

1.28×10^{-17} erg cm^{-2} s^{-1} deg^{-2}, respectively, corresponding to 81.8 per cent, 18.2 per cent, and ∼0.01 per cent of the flux in the Total model, which is 1.09×10^{-13} erg cm^{-2} s^{-1} deg^{-2}. The unresolved X-ray flux in the same band inferred by Lehmer et al. (2012) is $(3.05 \pm 2.25) \times 10^{-12}$ erg cm^{-2} s^{-1} deg^{-2}, while in the similar band (2–10) keV the unresolved CXB measured by Cappelluti et al. (2017) is $(6.47 \pm 0.82) \times 10^{-12}$ erg cm^{-2} s^{-1} deg^{-2}.

In the following we will present results only in the soft band, as those in the hard band are similar.

3.2 Auto power spectra

While it is difficult to measure directly the X-ray sources during the EoR due to their faint luminosities, it might be possible to probe them through the angular distribution of the CXB.

The angular auto power spectrum of the X-ray flux relates to the 3D power spectrum of X-ray sources, $P^s_X(k, z)$, through Limber's approximation[2] (Limber 1953):

$$C^s_X(l) = \int_{z>5} \mathrm{d}z \frac{H}{c d^2_{\rm com}} \Psi^s_X(z)^2 P^s_X(k = \frac{l}{d_{\rm com}}, z), \quad (8)$$

where $d_{\rm com}$ is the comoving distance from 0 to z, and

$$\Psi^s_X(z) = \frac{c}{4\pi} \frac{1}{H(z)(1+z)^2} \int_{\nu_{\rm min}(1+z)}^{\nu_{\rm max}(1+z)} \mathrm{d}\nu S^s(\nu, z) \mathrm{e}^{-\tau(\nu,z)}. \quad (9)$$

[2]Limber's approximation is consistent with the exact power spectrum at $l > 10$, while it breaks at lower l (see e.g. Simon 2007; Loverde & Afshordi 2008).

$P^s_X(k, z)$ is computed from the luminosity density of the X-ray sources contained in the snapshot of the simulation at z.

The angular power spectra $D^s_X(l) = l(l+1)C^s_X(l)/2\pi$ from the four models are shown in Fig. 3. The power spectrum of the ISM model displays an amplitude much lower than the others, consistently with its very low global flux showed in Fig. 2. Due to the rarity of BHs on the small scales, the power spectrum of the BH model approaches a white noise distribution with increasing l (i.e. $D^{\rm BH}_X \propto l^2$) and its amplitude is higher than the ones in the other models, although the global flux produced by BHs is lower than the one originating from XRBs (see Fig. 2). For the same reason, the power spectrum in the Total model is dominated by BHs. This can be clearly seen in the top panel of Fig. 3, where the power spectra have been calculated including all sources with an observed flux $< 2 \times 10^{-15}$erg cm^{-2} s^{-1}, to be compared to results from the XBOOTES survey (with a surface area of ∼9 deg^2; Kolodzig et al. 2017) that detected and removed sources with observed flux $> 2 \times 10^{-15}$erg cm^{-2} s^{-1}. Meanwhile, our predicted power spectra at all scales and in all models are much lower (below a few per cent) than the currently measured one.

If sources could be detected and removed in deep X-ray surveys down to a lower observed flux, the contribution from BHs would be reduced, without substantially changing the spectra of XRBs

Downloaded from https://academic.oup.com/mnras/article-abstract/480/1/26/5050917 by National and University Library of Iceland user on 03 October 2019

and ISM as they are dominated by fainter sources. The bottom panel in Fig. 3 refers to the case in which sources with an observed flux $> 7 \times 10^{-17}$erg cm^{-2} s^{-1} have been removed. Although at very small scales the power spectrum is still dominated by BHs, at $l <$ 3000 the Total model is now mainly determined by XRBs, and the impact of XRBs is expected to increase as more sources get removed. The power spectrum in the Total model is $\lesssim$2 per cent of the one measured by Cappelluti et al. (2013), who performed the same source subtraction in the deep *Chandra* ACIS-I AEGIS-XD survey that covered approximately 0.1 deg^2.

3.3 Cross-correlation with the 21 cm signal

In Eide2018a and Eide2018b we have seen that the hard UV and soft X-ray photons emitted by the sources considered here have a substantial impact on the physical properties of the IGM, in particular its temperature and HeIII content. In a companion paper, we will investigate their effect on the 21 cm signal, while here we concentrate specifically on its correlation with the CXB. As mentioned above, the photons contributing to the CXB in the bands studied here have energies higher than those in Eide2018a and Eide2018b, i.e. they are not responsible for the formation and evolution of highly ionized regions. On the other hand, the 21 cm signal is expected to correlate negatively with the X-ray sources located within highly ionized regions, since the XRBs, BHs, and hot ISM reside in the same galaxies hosting the stellar sources that drive IGM reionization. It should be noted that, while there is a one-to-one correlation between the sources of ionization and the CXB when this is dominated by XRBs, this is not strictly true for BHs as, despite still tracing highly ionized regions, there is not an active BH in each galaxy. In any case, such anticorrelation could be used to confirm the origin of the 21 cm signal, as well as give information on the properties of the X-ray sources during the EoR.

The 21 cm signal is typically described in terms of the differential brightness temperature, $\delta T_{21\rm cm}$, defined as (Furlanetto, Oh & Briggs 2006):

$$\delta T_{21\rm cm} = 28{\rm mK}(1+\delta)x_{\rm HI}\left(1-\frac{T_{\rm CMB}}{T_{\rm s}}\right)\left(\frac{1+z}{10}\right)^{1/2}, \quad (10)$$

where δ denotes the gas matter overdensity, $T_{\rm CMB} = 2.73(1+z)$ K is the CMB temperature at z, and $T_{\rm s}$ is the spin temperature. $\delta T_{21\rm cm}$ is calculated in each cell using the values of δ, $x_{\rm HI}$ and the kinetic temperature of the gas, T_k, obtained in the simulations, and assuming that $T_{\rm s} = T_k$.

The angular cross-power spectra of 21 cm brightness temperature and X-ray background are defined as $C^s_{\rm X-21cm}(z) \equiv \langle \widetilde{\delta T}_{21\rm cm} \widetilde{\delta F^s}^* \rangle$, where δF^s denotes the fluctuation of the X-ray background, while $\widetilde{\ }$ refers to the Fourier transfer. With Limber's approximation, the cross-power spectra are expressed as

$$C^s_{\rm X-21cm}(l,z) = \frac{H}{cd^2_{\rm com}}\Psi^s_{\rm X}(z)P^s_{\rm X-21cm}(k=\frac{l}{d_{\rm com}},z), \quad (11)$$

where $P^s_{\rm X-21cm}$ is the 3D cross-power spectrum of X-ray sources and 21 cm signal computed from the output of the RT simulations.

In the top panel of Fig. 4 we show the angular cross-power spectra at $z = 7$ and 9 for all simulations. At these redshifts the volume averaged H I fraction is $x_{\rm HI} \sim 0.24$ and 0.94, respectively, for all models, since the inclusion of more energetic sources has very little effect on the global hydrogen ionization fraction. It should be noted that here we only show a case in which X-ray sources with an observed flux larger than 10^{-17}erg cm^{-2} s^{-1} have been removed.

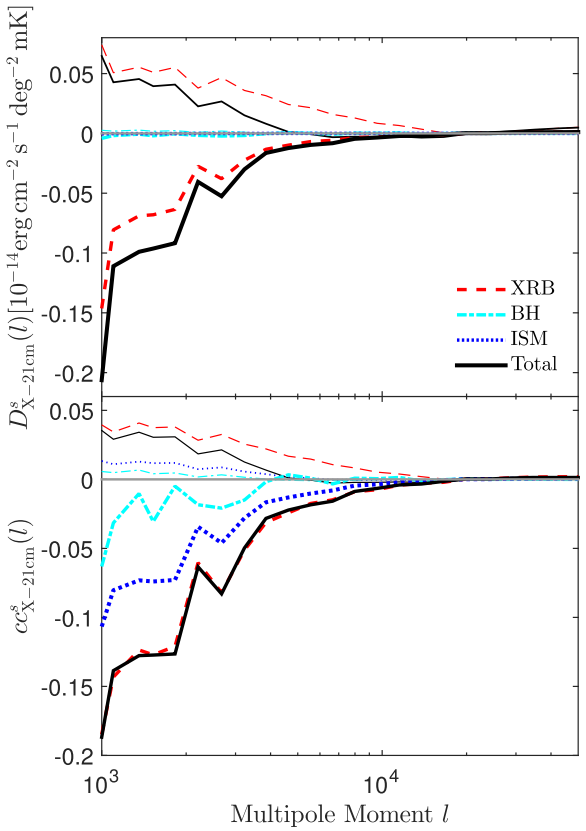

Figure 4. Cross-power spectra (top) and correlation coefficients (bottom) between the X-ray background and the 21 cm brightness temperature at $z = 7$ (thick lines), and 9 (thin) from the XRB (dashed red), BH (dash-dotted cyan), ISM (dotted blue), and Total (solid black) models. Note that X-ray sources with an observed flux larger than 10^{-17}erg cm^{-2} s^{-1} are removed. The gray solid horizontal line denotes the zero of the y-axis.

In the bottom panel of Fig. 4 we show the corresponding correlation coefficient factor, defined as

$$cc^s_{\rm X-21cm}(l,z) = \frac{C^s_{\rm X-21cm}(l,z)}{\sqrt{C^s_{\rm X}(l)\times C^s_{\rm 21cm}(l,z)}}, \quad (12)$$

where $C^s_{\rm X}$ is the integral X-ray power spectra at $z > 5$ (i.e. equation 8) and $C^s_{\rm 21cm}(l,z)$ is the angular power spectra of 21 cm brightness temperature at z.

For all models and at all redshifts, the correlations are significant only at $l < 10^4$, i.e. physical scales >5.6 cMpc ($k < 1.13$ Mpc^{-1}) at $z = 7$ and >6.0 cMpc ($k < 1.05$ Mpc^{-1}) at $z = 9$. At both redshifts, the cross-spectra in the ISM and BH models are much smaller than those in the XRB and Total models, consistently with their smaller global flux and angular power spectra (see Figs 2 and 3). At $z = 9$, when most of the IGM is still neutral, the 21 cm brightness temperature is dominated by the contribution from the overdensity and the spin temperature (see equation 10). As the sources of X-ray radiation mainly reside in overdense regions, the correlations are generally positive in all models, i.e. the X-ray radiation and the 21 cm signal during the early stage of reionization have a similar origin. Due to the higher X-ray radiation and stronger heating, the positive signal in the Total model is weaker than that in the XRB model. This behaviour is observed in both the power spectra and the correlation coefficients. At $z = 7$, when the IGM is highly ionized, a negative correlation is observed for all models, since the 21 cm brightness temperature in this case is more sensitive to the neutral

Downloaded from https://academic.oup.com/mnras/article-abstract/480/1/26/5050917 by National and University Library of Iceland user on 03 October 2019

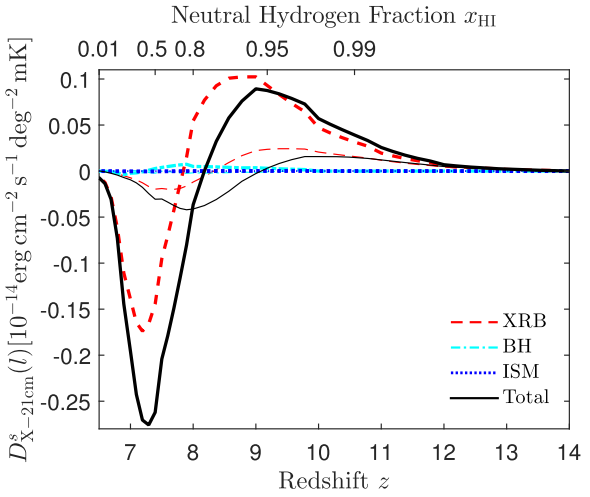

Figure 5. Redshift evolution of the cross-power spectra between the X-ray background and the 21 cm brightness temperature at $l = 1000$ (thick lines) and 5000 (thin) for the XRB (dashed red), BH (dash-dotted cyan), ISM (dotted blue), and Total (solid black) models.

hydrogen fraction that anticorrelates with the X-ray sources. Here the correlation is stronger than that at $z = 9$ because of the higher X-ray radiation at lower redshift.

Fig. 5 shows the redshift evolution of the cross-power spectra at $l = 1000$ ($k \approx 0.11$ Mpc^{-1} at $z = 7$) and 5000 ($k \approx 0.56$ Mpc^{-1} at $z = 7$) for the four models. As the amplitude of the cross-power spectra in the BH and ISM models is much lower than those in the XRB and Total models, we limit our discussion to the latter. The correlations are only significant at $z < 12$, because of the much lower X-ray flux at higher z. At $z > 9$, the cross-power spectra are positive at both $l = 1000$ and 5000, while negative at $z < 8$ where $x_{\rm HI} < 0.8$. The transition from positive to negative depends on the models, as well as the multipole moment l. In both models the transition happens earlier at $l = 5000$ than at $l = 1000$, since in a standard inside-out reionization scenario the smaller scales are ionized earlier. As the X-ray heating is stronger in the Total model than in the XRB model, this leads to the earlier transition of the Total model.

3.4 Detectability

The signal-to-noise ratio (S/N) for the cross-correlation power spectra at multiple l can be estimated by (Doré, Hennawi & Spergel 2004):

$$\left(\frac{S}{N}\right)^2 = \frac{f_{\rm sky}(2l+1)l_{\rm bin}C^2_{\rm X-21cm}}{(C_{\rm X}+N_{\rm X})(C_{\rm 21cm}+N_{\rm 21cm})+C^2_{\rm X-21cm}}, \quad (13)$$

where $f_{\rm sky}$ is the fraction of the sky covered by both the X-ray and 21 cm telescopes, $l_{\rm bin}$ is the bin width, $N_{\rm X}$ is the angular power spectrum of the X-ray foreground noise, and $N_{\rm 21cm}$ is the noise power spectrum of the 21 cm instrument. We assume $f_{\rm sky} = 0.0024$ (i.e. covered sky area $= 100$ deg^2) and $l_{\rm bin} \sim 0.46l$ (i.e. $(\log_{10}l)_{\rm bin} = 0.2$).

We adopt the X-ray foreground model by Helgason et al. (2014), which includes X-ray radiation from AGNs, hot gas, and galaxies (mostly dominated by XRBs). In this model, X-ray sources above a given flux limit $X_{\rm limit}$ are removed, assuming that they can be detected as point sources in deep X-ray surveys. For example, *Chandra* is able to detect point sources with measured flux above 6.4×10^{-18} erg cm^{-2} s^{-1} in the soft band with an exposure time ~ 7 Ms (Luo et al. 2017). Here, we take three flux limits: $X_{\rm limit} = 10^{-15}$, 10^{-16}, and 10^{-17} erg cm^{-2} s^{-1}. Correspondingly, we compute $C_{\rm X}$ and $C_{\rm X\text{-}21cm}$ in equation (13) by removing the sources brighter than those flux limits. While the instrument noise of X-ray facilities depends on the instrumental background and the exposure time, in the deep surveys it is expected to be much lower than the foreground contribution and/or to be removed in an efficient way (Cappelluti et al. 2013; Kolodzig et al. 2017), and thus we neglect it when estimating S/N.

We assume that the foreground contributions to the 21 cm signal can be accurately removed (see e.g. Koopmans et al. 2015). The noise power spectrum for the 21 cm instrument can be expressed as (Knox 1995)

$$N_{\rm 21cm} = [(1+z)/9.5)]^2\sigma^2_{\rm pix}\theta^2 {\rm e}^{l^2\theta^2/[8\ln(2)]}, \quad (14)$$

where $\sigma_{\rm pix}$ is the noise per pixel and θ is the full width at half maximum of the experimental beam. Using SKA[3] as our reference instrument, $\theta = 1$arcmin and $\sigma_{\rm pix} = 1$ mK at 150 MHz, corresponding to $\sim$1000 h of integration and 1 MHz of bandwidth (Koopmans et al. 2015).

Fig. 6 shows the predicted S/N for our four models and different X-ray flux limits. For $X_{\rm limit} = 10^{-15}$ erg cm^{-2} s^{-1}, S/N$<$1 for all models. When decreasing $X_{\rm limit}$ more point sources in the foreground contamination are removed, and thus the S/N increases. However, only models XRB and Total have S/N$\geq$1. As a reference, at $l = [1000, 2000]$ and $z = 7$ their S/N $\sim$2 for $X_{\rm limit} = 10^{-17}$ erg cm^{-2} s^{-1}, while S/N$\sim$1 for $X_{\rm limit} = 10^{-16}$ erg cm^{-2} s^{-1}. It is harder to detect the signal at higher redshifts (at $z = 9$ S/N$<$1 in all models) or at larger multipole moments, due to the weaker correlation.

Fig. 7 shows the cumulative S/N (from $l = 1000$) in our four models, which is evaluated as

$$\left(\frac{S}{N}\right)^2_{\rm cum} = \sum_{l=1000}^{l'} \frac{f_{\rm sky}(2l+1)C^2_{\rm X-21cm}}{(C_{\rm X}+N_{\rm X})(C_{\rm 21cm}+N_{\rm 21cm})+C^2_{\rm X-21cm}}. \quad (15)$$

$({\rm S/N})_{\rm cum}$ is mainly contributed by scales at $l < 10^4$, consistently with the weak X-ray and 21 cm correlations at $l \geq 10^4$ (see Fig. 4). At $z = 7$, the XRB and Total models have $({\rm S/N})_{\rm cum} \sim 3$ at $l' \geq 10^4$ in the case of $X_{\rm limit} = 10^{-17}$ erg cm^{-2} s^{-1}, while at $z = 9$ only the XRB model has $({\rm S/N})_{\rm cum} > 1$. With $X_{\rm limit} = 10^{-16}$ erg cm^{-2} s^{-1}, $({\rm S/N})_{\rm cum} \sim 1.2$ and 0.5 at $z = 7$ and 9.

Fig. 8 shows the evolution of the cumulative S/N from $l = 1000$–10^4 (i.e. $l' = 10^4$) in our four source models with different X-ray flux limits. For $X_{\rm limit} = 10^{-17}$ erg cm^{-2} s^{-1}, the correlations in the XRB and Total models can be measured in a wide redshift range from $z = 6.7$ to $\sim$9, with a peak $({\rm S/N})_{\rm cum} \sim 5$ at $z \sim 7.5$ where $x_{\rm HI} = 0.5$. For $X_{\rm limit} = 10^{-16}$ erg cm^{-2} s^{-1}, $({\rm S/N})_{\rm cum} \geq 1$ at $7 < z < 7.6$ in the XRB model and at $7 < z < 8.1$ in the Total model. It is impossible to measure the correlations for $X_{\rm limit} = 10^{-15}$ erg cm^{-2} s^{-1} as predicted by our four models.

We note here that the very deep *Chandra* survey, with a flux limit of 7×10^{-17} erg cm^{-2} s^{-1}, covers only an area of 0.1 deg^2 (Cappelluti et al. 2013), while 9 deg^2 are covered by a survey with a flux limit of only 2×10^{-15} erg cm^{-2} s^{-1} (Kolodzig et al. 2017). Then, such X-ray surveys are not expected to be able to measure the X-ray and 21 cm correlation. A much larger area of 140 deg^2 is expected to be covered by eROSITA,[4] but also in this case

[3] https://www.skatelescope.org
[4] http://www.mpe.mpg.de/eROSITA

Downloaded from https://academic.oup.com/mnras/article-abstract/480/1/26/5050917 by National and University Library of Iceland user on 03 October 2019

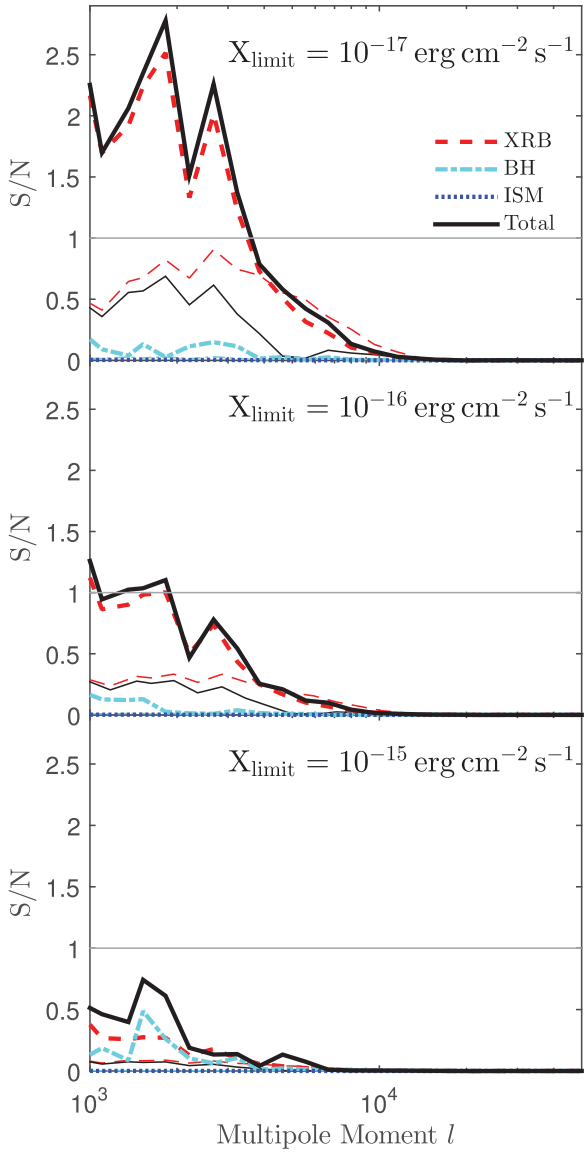

Figure 6. S/N for X-ray flux limits of 10^{-17} (top panel), 10^{-16} (center), and 10^{-15} (bottom) erg cm^{-2} s^{-1} in model XRB (dashed red lines), BH (dash-dotted cyan), ISM (dotted blue), and Total (solid black) at $z = 7$ (thick lines) and $z = 9$ (thin). The gray solid horizontal line denotes S/N=1.

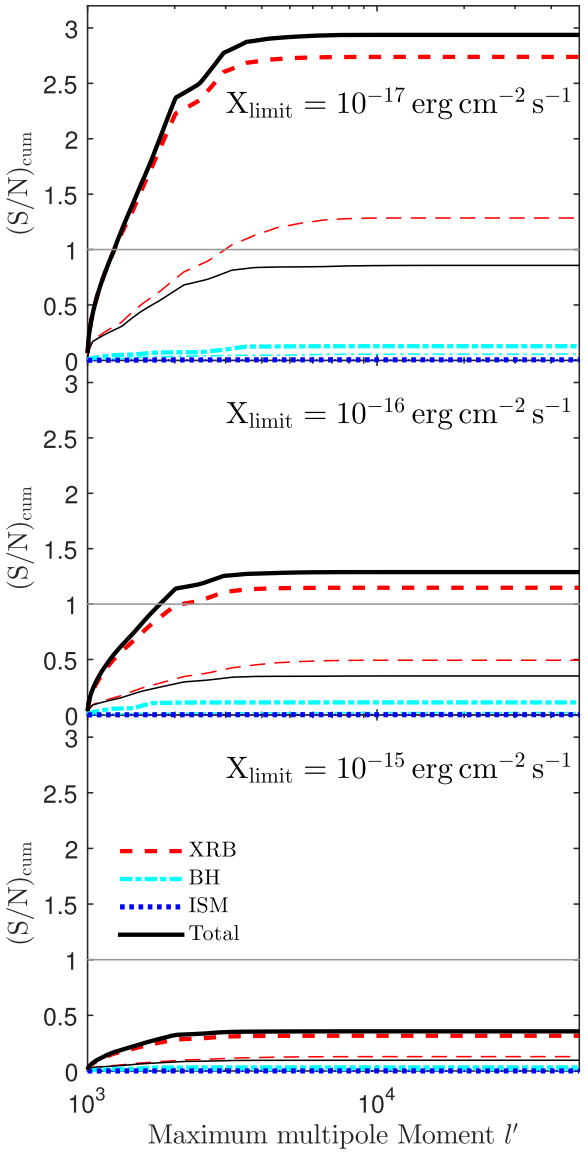

Figure 7. Cumulative S/N as a function of the maximum multipole moment l' with X-ray flux limits of 10^{-17} (top panel), 10^{-16} (center), and 10^{-15} (bottom) erg cm^{-2} s^{-1} for model XRB (dashed red lines), BH (dash-dotted cyan), ISM (dotted blue), and Total (solid black) at $z = 7$ (thick lines) and $z = 9$ (thin). The gray solid horizontal line denotes S/N=1.

sources fainter than 2.9×10^{-15} erg cm^{-2} s^{-1} would not be resolved (Merloni et al. 2012). More promising is the ATHENA[5] mission, with a flux limit of $\sim 10^{-16}$ erg cm^{-2} s^{-1} expected for a survey area of 100 deg^2 (J. Aird, private communication; Aird et al. 2013). The proposed *LYNX* telescope[6] should also be able to measure such correlation, thanks to its designed high resolution. Deep $\sim$1000 h integration is considered for SKA on five separate 20 deg^2 windows covering a total of 100 deg^2 (Koopmans et al. 2015).

4 DISCUSSION AND CONCLUSIONS

We used the high-resolution cosmological hydrodynamical simulation MassiveBlack-II (Khandai et al. 2015) post-processed with RT calculations (Eide2018a,b) to investigate the high-z component of the cosmic X-ray background (CXB) and its correlation with the 21 cm signal from the EoR. We have considered four models with contribution from different source types: X-ray binaries (XRB) (Fragos et al. 2013b; Madau & Fragos 2017), accreting nuclear BH (Shakura & Sunyaev 1973; Krawczyk et al. 2013), hot interstellar medium (ISM) (Mineo et al. 2012; Pacucci et al. 2014) and a case that includes all the above sources combined (Total). The X-ray sources are treated in the RT simulations together with the UV radiation from stars.

We found that the global X-ray flux increases rapidly with decreasing redshift, due to the fast growing of star formation. The global flux in both the soft (0.5–2) keV and hard (2–8) keV X-ray bands at $z > 5$ is dominated by the XRBs ($\sim$80 per cent of the Total model), while the BHs and the ISM contribute only $\sim$20 per cent and $<$1 per cent, respectively.

[5] http://www.the-athena-x-ray-observatory.eu
[6] https://wwwastro.msfc.nasa.gov/lynx

Downloaded from https://academic.oup.com/mnras/article-abstract/480/1/26/5050917 by National and University Library of Iceland user on 03 October 2019

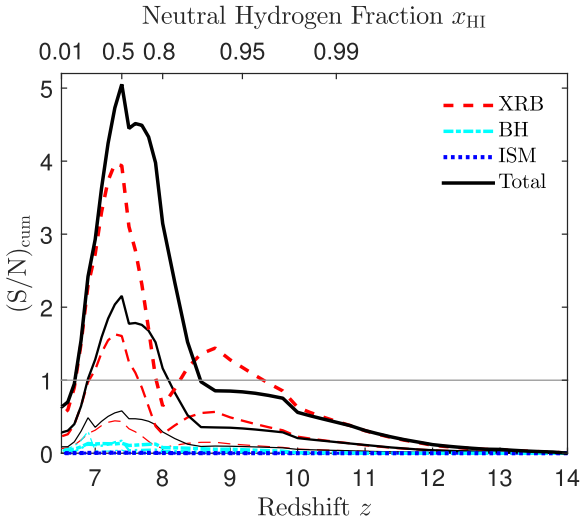

Figure 8. Cumulative S/N from $l = 1000$–10^4 as a function of redshift (or hydrogen neutral fraction) for X-ray flux limits 10^{-17} (thick lines), 10^{-16} (normal), and 10^{-15} (thin) erg cm^{-2} s^{-1} in the model XRB (dashed red lines), BH (dash-dotted cyan), ISM (dotted blue), and Total (solid black). The gray solid horizontal line denotes S/N=1.

As BHs have a very low number density but a high luminosity, they display a shot noise like power spectrum, with an amplitude much higher than that of XRBs and ISM. However, if bright sources could be identified in deep X-ray surveys and removed, the shot noise spectrum of BHs would be strongly reduced (Helgason et al. 2014). The ISM contribution is always negligible.

We found that the correlation between the CXB and the 21 cm signal is significant at $l < 10^4$, while it is almost zero at larger l. The correlations are positive at high z when most of the gas is in a neutral state and the overdensity distribution dominates the signal, while they become negative once most of the hydrogen becomes ionized. The transition from a positive to a negative correlation depends on both the X-ray model and the angular scale considered, i.e. it happens earlier in models in which the X-ray flux is stronger and on scales ionized earlier (the smaller scales). As a reference, the transition in the Total model happens at $z = 9.1$ and 8.2 for $l = 5000$ and 1000, respectively, while in the XRB model the transition at the same scales happens at $z = 8.3$ and 7.8, respectively.

The detectability of the X-ray and 21 cm correlations is highly sensitive to the resolution of the X-ray surveys, as the noise level expected for the deep surveys planned by SKA is much smaller than the power spectrum and thus is not expected to affect the measurements. We found that if the X-ray survey is deep enough to remove the bright sources with an observed flux $> 10^{-17}$ erg cm^{-2} s^{-1}, the cumulative signal-to-noise ratio $(S/N)_{\rm cum}$ from $l = 1000$–10^4 would be $\sim$5 at $x_{\rm HI} = 0.5$, and $\sim$2 if the sources with observed flux $> 10^{-16}$ erg cm^{-2} s^{-1} are removed, while if only sources with observed flux $> 10^{-15}$ erg cm^{-2} s^{-1} are removed, the correlations could not be measured. It will also be crucial to cover a large enough survey area to obtain a high S/N, although this requires longer total exposure time for both the X-ray and 21 cm facilities. Such large area surveys would allow to measure the correlations also at scales of $l < 1000$ (not covered by our simulations), where the X-ray background and 21 cm signals are still expected to correlate (Liang et al. 2016).

Although different models and approaches are adopted, our conclusions have a broad agreement to those in Liang et al. (2016), especially with regard to the specific behaviour of the evolution of X-ray background and the 21 cm signal correlations.

Our predicted CXB from the EoR is much lower than what has been observed, in terms of both global X-ray flux (less than a few per cent of the one measured by Cappelluti et al. 2017 and the one inferred by Lehmer et al. 2012) and power spectrum of fluctuations ($\lesssim$2 per cent of those measured by Cappelluti et al. 2013 and Kolodzig et al. 2017). This suggests that the X-ray contribution from high-z energetic sources could be larger than the one considered here, leaving some freedom in the choice of some parameters adopted in the simulation. In particular, the BHs properties and distribution at these redshifts are strongly dependent on the seeding procedure adopted in the hydrodynamical simulations (see Eide2018a and Eide2018b for a discussion) and a different procedure could easily increase their contribution without violating observational constraints (Salvaterra et al. 2007).

In conclusion, the X-ray radiation and 21 cm signal during the EoR show significant correlations, which could be used in the future to reduce systematic effects in either X-ray or 21 cm data, as well as to confirm the cosmological origin of the 21 cm signal and to help constraining the properties of X-ray sources during the EoR. The combination of the planned 21 cm experiment SKA and X-ray facilities such as LYNX and ATHENA in the near future have the potential to measure such correlations with a meaningful S/N.

ACKNOWLEDGEMENTS

The authors are grateful to James Aird, Andrea Merloni, Arne Rau, and Mara Salvato for inputs on planned X-ray surveys, Ruben Salvaterra for useful comments, and an anonimous referee for his or her comments. The tools for bibliographic research are offered by the NASA Astrophysics Data Systems and by the JSTOR archive. QM is supported by the National Basic Research Program ("973" Program) of China (grant No. 2014CB845800), the National Natural Science Foundation of China (grant Nos 11673068 and 11725314), the Youth Innovation Promotion Association (2011231), the Key Research Program of Frontier Sciences (QYZDB-SSW-SYS005), the Strategic Priority Research Program 'Multiwaveband gravitational wave Universe' (grant No. XDB23000000) of the Chinese Academy of Sciences. MBE thanks the Astronomy and Astrophysics department at UCSC for their kind hospitality and is a fellow of the U.S.-Norway Fulbright Foundation. KH acknowledges support from the Icelandic Research Fund, grant number 173728-051.

REFERENCES

Aird J. et al., 2013, preprint (arXiv:1306.2325)
Brandt W. N., Hasinger G., 2005, ARA&A, 43, 827
Cappelluti N. et al., 2012, MNRAS, 427, 651
Cappelluti N. et al., 2013, ApJ, 769, 68
Cappelluti N. et al., 2017, ApJ, 837, 19
Christian P., Loeb A., 2013, J. Cosmol. Astropart. Phys., 9, 014
Ciardi B., Ferrara A., Marri S., Raimondo G., 2001, MNRAS, 324, 381
Comastri A., Setti G., Zamorani G., Hasinger G., 1995, A&A, 296, 1
Dijkstra M., Haiman Z., Loeb A., 2004, ApJ, 613, 646
Doré O., Hennawi J. F., Spergel D. N., 2004, ApJ, 606, 46
Eide M. B., Graziani L., Ciardi B., Feng Y., Kakiichi K., Di Matteo T., 2018, MNRAS,
Fernandez E. R., Zaroubi S., Iliev I. T., Mellema G., Jelić V., 2014, MNRAS, 440, 298
Fialkov A., Barkana R., Visbal E., 2014, Nature, 506, 197
Fialkov A., Cohen A., Barkana R., Silk J., 2017, MNRAS, 464, 3498

Downloaded from https://academic.oup.com/mnras/article-abstract/480/1/26/5050917 by National and University Library of Iceland user on 03 October 2019

Fragos T., Lehmer B. D., Naoz S., Zezas A., Basu-Zych A., 2013b, ApJ, 776, L31
Fragos T. et al., 2013a, ApJ, 764, 41
Furlanetto S. R., Oh S. P., Briggs F. H., 2006, Phys. Rep., 433, 181
Graziani L., Ciardi. B., Glatzle M., 2018, preprint (arXiv: 1805.11615)
Graziani L., Maselli A., Ciardi B., 2013, MNRAS, 431, 722
Helgason K., Cappelluti N., Hasinger G., Kashlinsky A., Ricotti M., 2014, ApJ, 785, 38
Khandai N., Di Matteo T., Croft R., Wilkins S., Feng Y., Tucker E., DeGraf C., Liu M.-S., 2015, MNRAS, 450, 1349
Knox L., 1995, Phys. Rev. D, 52, 4307
Kolodzig A., Gilfanov M., Hütsi G., Sunyaev R., 2017, MNRAS, 466, 3035
Kolodzig A., Gilfanov M., Hütsi G., Sunyaev R., 2018, MNRAS, 473, 4653
Komatsu E. et al., 2011, ApJS, 192, 18
Koopmans L. et al., 2015, Advancing Astrophysics with the Square Kilometre Array (AASKA14), p. 1
Krawczyk C. M., Richards G. T., Mehta S. S., Vogeley M. S., Gallagher S. C., Leighly K. M., Ross N. P., Schneider D. P., 2013, ApJS, 206, 4
Lehmer B. D. et al., 2012, ApJ, 752, 46
Liang J.-M., Mao X.-C., Qin B., 2016, Res. Astron. Astrophys., 16, 132
Limber D. N., 1953, ApJ, 117, 134
Loverde M., Afshordi N., 2008, Phys. Rev. D, 78, 123506
Luo B. et al., 2017, ApJS, 228, 2
Madau P., Fragos T., 2017, ApJ, 840, 39
Maselli A., Ciardi B., Kanekar A., 2009, MNRAS, 393, 171
Maselli A., Ferrara A., Ciardi B., 2003, MNRAS, 345, 379
Merloni A. et al., 2012, preprint (arXiv:1209.3114)
Mesinger A., Ferrara A., Spiegel D. S., 2013, MNRAS, 431, 621
Mineo S., Gilfanov M., Sunyaev R., 2012, MNRAS, 426, 1870
Mitchell-Wynne K., Cooray A., Xue Y., Luo B., Brandt W., Koekemoer A., 2016, ApJ, 832, 104
Moretti A., Vattakunnel S., Tozzi P., Salvaterra R., Severgnini P., Fugazza D., Haardt F., Gilli R., 2012, A&A, 548, A87
Pacucci F., Mesinger A., Mineo S., Ferrara A., 2014, MNRAS, 443, 678
Salvaterra R., Ciardi B., Ferrara A., Baccigalupi C., 2005, MNRAS, 360, 1063
Salvaterra R., Haardt F., Volonteri M., 2007, MNRAS, 374, 761
Shakura N. I., Sunyaev R. A., 1973, A&A, 24, 337
Shan H.-Y., Qin B., 2009, Res. Astron. Astrophys., 9, 73
Simon P., 2007, A&A, 473, 711
Verner D. A., Ferland G. J., Korista K. T., Yakovlev D. G., 1996, ApJ, 465, 487
Xu H., Ahn K., Norman M. L., Wise J. H., O'Shea B. W., 2016, ApJ, 832, L5
Yamamoto K., Sugiyama N., 1998, Phys. Rev. D, 58, 103508
Śliwa W., Soltan A. M., Freyberg M. J., 2001, A&A, 380, 397

This paper has been typeset from a TEX/LATEX file prepared by the author.

Downloaded from https://academic.oup.com/mnras/article-abstract/480/1/26/5050917 by National and University Library of Iceland user on 03 October 2019